Chapter 12

SENSING PROTEINS WITH ADAPTIVE METAL NANOSTRUCTURES

VLADIMIR P. DRACHEV, MARK D. THORESON, and VLADIMIR M. SHALAEV
Purdue University

1. INTRODUCTION

Raman scattering spectra enable molecular "fingerprinting," which is of particular interest for molecule sensing and bio-applications. Surface enhanced Raman scattering (SERS) provides greater detection sensitivity than conventional Raman spectroscopy,[1-3] and it is quickly gaining traction in the study of biological molecules adsorbed on a metal surface.[4-12] SERS spectroscopy allows for the detection and analysis of minute quantities of analytes because it is possible to obtain high-quality SERS spectra at sub-monolayer molecular coverage as a result of the large scattering enhancements. SERS has also been shown to be sensitive to molecular orientation and to the distance from the metal surface.[13]

The SERS enhancement mechanism originates in part from the large local electromagnetic fields caused by resonant surface plasmons that can be optically excited at certain wavelengths for metal particles of different shapes or closely spaced groups of particles.[14-21] For aggregates of interacting particles, which are often structured as fractals, plasmon resonances can be excited in a very broad spectral range.[22] In addition to electromagnetic field enhancement, metal nanostructures and molecules can form charge-transfer complexes that provide further enhancement for SERS.[23-29] The resulting overall enhancement depends critically on the particle or aggregate nanostructure morphology,[22,30-36] and it can be as high

as 10^5 to 10^9 for the area-averaged macroscopic signal and 10^{10} to 10^{15} within the local resonant nanostructures.

A variety of structures have been found to be appropriate for SERS, including roughened metal electrodes,[1-3] aggregated films,[15] metal islands of different morphologies,[14,15,17-20] and semicontinuous metal films near the percolation threshold.[37-39] Among SERS-active substrates, vacuum-evaporated nanostructured metal films are well suited for SERS mechanism studies and have a high potential for applications.[14-20,24,39-43] The effect on the metal film due to deposition rate, mass thickness, and thermal annealing were studied in detail previously.[18, 40-43]

The most advanced tendency in SERS is to engineer optimal nanostructures with a controlled particle shape, such as triangles,[35,44] nanoshells,[36,45] or with a regular arrangement achieved by nanosphere lithography,[35] electron beam lithography,[46] or through metal coating of dielectric spheres.[4,42] It has been shown that the maximum local field can be obtained between a pair of particles with an appropriate shape like a bow-tie structure[47,48] fabricated with electron beam lithography or nanosphere lithography. In particular, the largest macroscopic enhancement factor related to unit area covered with metal was reported with an array of triangle particles.[35] Strong SERS enhancement can also occur in a periodic array of metal nanoparticles.[80]

We found recently that vacuum evaporated silver films fabricated at a certain range of evaporation parameters allow fine rearrangement of their local structure under protein deposition.[49-53] Such a substrate, which is referred to as *adaptive*, provides large SERS enhancement that allows protein sensing at monolayer protein surface density and enables adsorption of proteins without significant changes in their conformational states. This adaptive property appears to be especially important for the sensing of large molecules whose size is comparable with the typical sizes of the metal film nanostructure (particle size, interparticle spacing). In the case of proteins of about nanometer size, it is still an issue to match an optimal design of engineered nanostructures with a molecule of particular size and shape. This issue can be addressed with adaptive nanostructures where protein-mediated restructuring forms groups of metal particles naturally covered and matched with the molecules of interest.

In this chapter we discuss specific properties of adaptive silver films (ASFs) and provide several examples of their uses for protein sensing and potential applications in protein microarrays. An example of SERS spectral sensitivity to protein conformational state is presented in the case of insulin. We also describe further development of this type of substrate to improve the SERS signal by addition of a sublayer of bulk metal.

2. BASIC FORMULAS FOR SERS ENHANCEMENT FACTOR

The concept of the enhanced local field in aggregated particle films based on the Maxwell-Garnett approach was applied to SERS in the 1980s.[14-15,17-19] These theories account for particle shape and, in a strongly simplified manner, particle interactions. The early theories also emphasize that strong local fields can only result from large field fluctuations.[16]

In many cases, aggregates of metal particles form fractal structures, which are characterized by a scale-invariant distribution such that they look similar at different length scales. A special type of fractal structure is represented by a percolation film (also referred to as a semicontinuous metal film). A percolation film is formed by fractal metal clusters of different sizes, from a cluster of a single or just few particles up to the "infinite" fractal cluster that spans over the whole film and provides a conducting (percolating) path for the film. Below the percolation threshold a metal-dielectric film is an insulator whereas above the threshold it is a conductor. Although macroscopically a percolation film is homogeneous, the metal clusters can still be characterized by a scale-invariant distribution.

For fractal systems, the powerful scaling approach can be applied. A theory describing optical properties of fractal aggregates was developed by Shalaev and Stockman,[22,39] and an optical theory of percolation composites was put forward by Sarychev and Shalaev.[38,39] There is much in common between fractal aggregates and percolation films; in both cases, the electromagnetic excitations are localized in small, nanometer-sized areas which are referred to as "hot spots." The local-field intensity in the hot spots can exceed the intensity of an incident wave by three to five orders of magnitude, resulting in a dramatic Raman scattering enhancement of up to twelve orders of magnitude under optimum conditions.

This enhancement results from the excitation of local plasmon modes in aggregates (clusters) of metal nanoparticles. Because of scale-invariance, metal clusters in fractal and percolation systems are characterized by a large variety of shapes and sizes. Different local structures formed by metal particles resonate at different frequencies so that all together they provide a broad range of enhancement for Raman scattering. Because different metal clusters resonate at different frequencies, the hot spots at different frequencies are spatially separated. A typical size of the hot spots is between 10 to 100 nm. Light at a given frequency excites a different distribution of the hot spots on a fractal or percolation system. The resonant plasmon modes in such systems cover a very broad spectral range from the near-UV to the mid-IR.

In many cases, random aggregates of particles do not form fractal or percolation systems (for example, an island film well below the percolation). Still, hot spots are excited in various small groups of metal particles and the optical properties of such random systems are often similar to those obtained for fractal and percolation systems. In fact, it has been shown[38,39] that the optical scaling theory developed for percolation systems works well in a rather broad range of metal concentrations around the percolation threshold, including those well below and above the percolation threshold. For optical frequencies, the scaling formulas of the Shalaev-Sarychev theory remain valid in a broad range of metal filling factors, roughly from 0.3 to 0.7. The fractal theory[39] is also very robust and describes random aggregates of particles (even if they are not fractal), provided that there is frequency-spatial selectivity so that hot spots at different frequencies are located in different locations, resulting in an inhomogeneously-broadened distribution of plasmon modes (see Section 3.6.1 of Ref. [39]).

Below we present formulas describing SERS enhancement in random metal-dielectric composites, including the important case of metal-dielectric films.

2.1 Enhancement factor for Raman scattering

Let's assume that Raman-active molecules are placed on a metal-dielectric film, where the plasmon modes can be excited resulting in local-field enhancement. Raman scattering (RS) of an incident wave at frequency ω results in a scattered field at a shifted frequency ω_s. The shift $\omega - \omega_s$ is equal to one of the molecule's vibrational frequencies, and the combination of all such vibrational frequencies represents the molecule's "fingerprint." Spontaneous Raman scattering is a linear, incoherent optical process. Because the plasmon modes cover a very broad spectral range, the fields at frequencies ω and ω_s can both experience the enhancement caused by the resonant plasmon modes.[16] As a result, the enhancement factor for surface-enhanced Raman scattering (SERS) is given by the product of the enhancements for the two fields at frequencies ω and ω_s: [39]

$$G_{RS} \sim \left\langle \left| \frac{E_\omega}{E_\omega^0} \right|^2 \left| \frac{E_{\omega_s}}{E_{\omega_s}^0} \right|^2 \right\rangle, \qquad (1)$$

where the angular brackets stand for spatial averaging over the random film. In Equation (1), E_ω and $E_{\omega s}$ are the local enhanced fields at frequencies ω and ω_s, respectively, whereas E_ω^0 and $E_{\omega s}^0$ are the probe, non-enhanced fields at

these frequencies. Below, for simplicity, we set these non-enhanced amplitudes both equal to unity so that $|E_\omega|^2$ and $|E_{\omega s}|^2$ represent the local enhancements for the field intensities at frequencies ω and ω_s. Then, the enhancement factor for RS in Eq. (1) can be rewritten as

$$G_{RS} \sim \left\langle \left| E_\omega E_{\omega_s} \right|^2 \right\rangle . \tag{2}$$

There are two important limiting cases for Eq. (2) that we consider below. If the Stokes frequency shift is smaller than the plasmon resonance width Γ, then the hot spots at the two frequencies occur in the same spatial positions so that the enhancement can be written as

$$G_{RS} \sim \left\langle |E|^4 \right\rangle , \tag{3}$$

where the ω and ω_s fields have been set equal to each other because the two enhancements are fully correlated. Thus under these optimum conditions, the SERS enhancement is proportional to the fourth power of the enhanced local field averaged over the film. Such nonlinear dependence for the *enhancement* should not be confused with the Raman signal itself, which is still proportional to the field intensity because it is a linear process.

A more conventional situation, however, is represented by the case when the shift $\omega - \omega_s$ exceeds the plasmon resonance width Γ. For large shifts, the positions of the hot spots at the two frequencies can be approximated as statistically independent. Then, we can decouple the averaging for the two fields in Eq. (2) and present the enhancement as

$$G_{RS} \sim \left\langle |E_\omega|^2 \right\rangle \left\langle \left| E_{\omega_s} \right|^2 \right\rangle . \tag{4}$$

Eq. (4) is in agreement with experiments[15,18] and theory[17-18] showing that the enhanced Raman intensity is proportional to the product of the absorptions at the laser and scattered frequencies, i.e. to $A(\omega)A(\omega_s)$[15,17-19] (note that the absorption A is proportional to $\langle |E|^2 \rangle$). This fact helps in evaluating various substrates for their possible use as SERS substrates.

For noble and coinage metals, the dielectric permittivity can be well-described by the Drude formula

$$\varepsilon = \varepsilon_o - \frac{\omega_p^2}{\omega\left(\omega + i\tau^{-1}\right)}, \tag{5}$$

where $\tau = \Gamma^{-1}$ is the relaxation time for plasmon oscillations, ε_0 is the interband contribution to the permittivity and ω_p is the bulk plasma frequency. For effective SERS metals the parameters above have the following magnitudes:[54,55] Ag (ω_p= 9.1 eV, τ_{eff}^{-1} = 0.021 eV), Au (ω_p= 9.0 eV, τ_{eff}^{-1} = 0.066 eV), and Cu (ω_p= 8.8 eV, τ_{eff}^{-1} = 0.09 eV).

2.2 Relationship between electromagnetic enhancement factor and effective optical properties

Below we estimate the SERS enhancement factor, using formulas obtained for fractal and percolation systems.[22,38,39] As mentioned, these results remain approximately valid for a rather broad class of metal-dielectric composites and films.

For fractals, the enhancement for a nonlinear process which is proportional to the n^{th} power of the local field is estimated as[39]

$$\left\langle |E|^n \right\rangle_{frac} \sim \left(\frac{|\varepsilon'|^2}{\varepsilon'' \varepsilon_h} \right)^{n-1} \sim \left(\frac{\omega_p^2}{\omega} \tau \right)^{n-1}. \tag{6}$$

For the latter estimate we used the Drude formula given by Eq. (5) and the dielectric permittivity of the host materials ε_h was estimated as $\varepsilon_h \sim 1$. There is also a frequency-independent pre-factor in Eq. (6) which depends on the specific geometry of the system; for the sake of the simplicity we omit it here.

For a percolation system, the enhancement factor is given by

$$\left\langle |E|^n \right\rangle_{perc} \sim \left[\left(\frac{|\varepsilon'|}{\varepsilon_h} \right)^{\frac{\nu(n-2)+s}{t+s}} \right] \left(\frac{|\varepsilon'|}{\varepsilon''} \right)^{(n-1)(1-2\gamma)+\gamma}, \tag{7}$$

where ν, t, s, and γ are the critical exponents of the percolation theory. We use the fact that for 2D systems $\nu = t = s = 4/3$ and set $\gamma = 0$ for simplicity (γ takes into account the presence of delocalized modes[56]). Then, by applying the Drude formula (Eq. 6) and taking $\varepsilon_h \sim 1$., we have

$$\left\langle |E|^n \right\rangle_{perc} \sim \left[\frac{|\varepsilon'|^{3/2}}{\varepsilon_h \varepsilon''} \right]^{n-1} \sim \left(\omega_p \tau\right)^{n-1}. \quad (8)$$

By using Eqs. (3)-(6), we obtain the SERS enhancement in fractal systems for the two limiting cases of small and large Stokes shifts,

$$G_{RS}^{(frac)}(\omega - \omega_s \lesssim \Gamma) \sim c\left(\frac{|\varepsilon'|^2}{\varepsilon'' \varepsilon_h} \right)^3 \sim c\left(\frac{\omega_p^2}{\omega} \tau \right)^3 \quad (9)$$

and

$$G_{RS}^{(frac)}\left(\omega - \omega_s >> \Gamma\right) \sim c\left(\frac{|\varepsilon'|^2}{\varepsilon'' \varepsilon_h} \right)^2 \sim c\left(\frac{\omega_p^2}{\omega} \tau \right)^2, \quad (10)$$

where we added the geometry-dependent pre-factor c, which is estimated to be in the range of 10^{-1} to 10^{-2} (it can have different values in Eqs. 9 and 10).

For percolation systems, Eqs. (3)-(5) and (8) result in the following SERS enhancement factors for large and small Stokes shifts, respectively,

$$G_{RS}^{(perc)}(\omega - \omega_s \lesssim \Gamma) \sim c\left(\frac{|\varepsilon'|^{3/2}}{\varepsilon_h \varepsilon''} \right)^3 \sim c\left(\omega_p \tau\right)^3 \quad (11)$$

and

$$G_{RS}^{(perc)}\left(\omega - \omega_s >> \Gamma\right) \sim c\left(\frac{|\varepsilon'|^{3/2}}{\varepsilon_h \varepsilon''} \right)^2 \sim c\left(\omega_p \tau\right)^2, \quad (12)$$

where the geometry factor c has been included.[39] Although the values of factor c can be different in Eqs. (9)-(12), in all cases it is frequency independent and estimated to be in the range of 1 to 10^{-3}.

The enhancement factors for fractal and percolation systems are similar and differ by the factor ω_p/ω, which is about 4 for the visible range. Although these estimates were obtained for the special case of scale-

invariant systems such as fractal and percolation systems, they remain approximately valid for many systems of randomly distributed clusters of metal particles including island films or colloidal aggregates. In all of these systems, the enhanced local fields are concentrated in randomly distributed hot spots whose spatial positions depend on the frequency of the driving field.

It is also important to mention that the macroscopic, average electromagnetic enhancement of Raman scattering is larger for Ag than for Au or Cu, which follows from the formulas above and the optical constants for these metals. According to Eqs. (9)-(12) and the optical constants given above, the macroscopic SERS enhancement can range between 10^4 and 10^9. The local enhancement in the hot spots can be one to three orders of magnitude larger and thus reaches 10^{10} or even 10^{12} for optimal conditions. SERS enhancement factor with larger than these magnitudes can occur when a chemical enhancement mechanism is also present, which can provide an additional "boost" to the overall SERS enhancement. The chemical enhancement factor ranges typically from 10 to 10^3. Therefore, under optimal conditions when both the electromagnetic and chemical mechanisms contribute, the SERS enhancement can be as high as 10^{15}.

3. ADAPTIVE PROPERTY OF SILVER FILMS

As we mentioned above, vacuum evaporated silver films fabricated at a certain range of evaporation parameters allow fine rearrangement of their nanostructure under protein deposition in buffer solution. Although all of the surface physical and chemical processes resulting in the restructuring are not yet fully established, we have used several methods to study the restructuring mechanism. The changes in the film nanostructure, color, and other properties have been studied by optical methods, including UV-Vis spectrophotometry and Raman spectroscopy. We have also employed such analysis as field emission scanning electron microscopy (FE SEM), adhesion testing, atomic force microscopy, X-ray photoemission spectroscopy, and X-ray diffractometry as well.

The adaptive silver films (ASFs) are typically formed on a dielectric substrate under vacuum evaporation with an electron beam with an initial pressure inside the system of approximately 10^{-7} Torr (see details in Ref [49]). The dielectric (glass) slides were covered first by a sublayer of 10 nm of SiO_2 followed by an 8-13 nm Ag layer deposited at a rate of 0.05 nm/s. During the silver deposition process, small isolated metal granules are formed first on the dielectric substrate. As the silver coverage increases, the granules coalesce, resulting in various sizes of silver particles and their

aggregates. Qualitative estimates of adhesion performed with the common tape test[57] show good adhesion for the Ag/SiO_2/glass substrate structure. Absorption and reflection measurements before and after the tape test indicate the relative level of adhesion of the film to the glass substrate. The changes in absorption/reflection spectra after the tape test were less than 5% for the Ag/SiO_2/glass substrate. A comparison of silver substrates with and without a SiO_2 sub-layer shows that adhesion of silver on glass is poor. In the case of very high adhesion (such as when an adhesion-promoting titanium sublayer is included), the deposition of the protein solution does not lead to spot color changes nor structural modifications, and typically little or no SERS is observed.

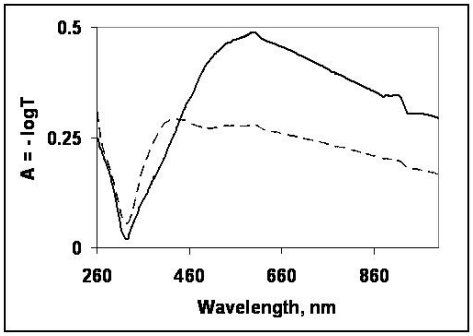

Figure 12-1. Absorption (extinction) spectra for a typical ASF substrate, solid line – bare ASF substrate, dashed line – inside insulin spot on an ASF substrate.

Excitation of the collective electron oscillations (plasmons) in a metal nanostructure results in strong light and metal particle interactions and eventually in increased absorption relative to a thick metal film. Typical absorbance and reflectance spectra of an ASF substrate are similar in shape and have a maximum at around 500 nm with a broad wing into the longer wavelengths (see Fig. 12-1, solid line). Reflection is typically comparable or slightly larger than absorption by a factor of roughly 1-1.4 when both spectra are expressed in percent. Both the visible color of the film and the extinction spectrum change after protein deposition, as is shown in Fig. 12-1 (dashed line) for an insulin spot. The spectrum inside the analyte spot typically shows a blue-shifted maximum, reduced slope of the long wavelength wing, and reduced extinction integrated over the 300 nm to 1100 nm spectral range. An FE SEM image of the same insulin spot (Fig. 12-2b) clearly shows nanoscale restructuring, where groups of closely spaced metal nanoparticles

are formed. This is in contrast to the film outside the spot, where rather disintegrated particles are typical (Fig. 12-2a).

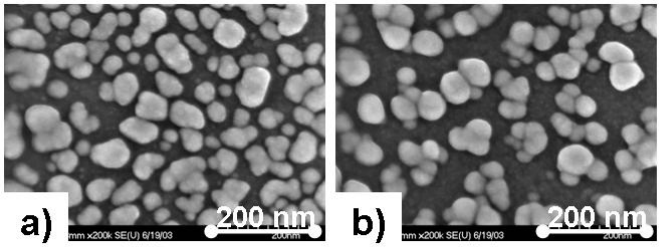

Figure 12-2. FE SEM images of an ASF substrate outside (a) and inside (b) an insulin spot.

A representative view of an ASF substrate after protein deposition and drying is shown in Fig. 12-3a. Note that after washing with a Tris-buffered saline (TBS) solution containing 0.5% Tween-20, the silver coating has been removed everywhere except the areas under the analyte spots, as clearly seen in Fig. 12-3b. From this one can conclude that the proteins stabilize the silver film, allowing the silver film to remain in place even through washing procedures. This indicates that the biomolecules themselves play a key role in forming a stable complex with the silver particles. By varying the biomolecule and buffer concentrations, we observe that both factors are important in the formation of uniform, stabilized analyte spots. A lower protein concentration (by roughly a factor of 10-20) in a deposition solution results in an almost transparent spot and hence no metal particles. The solvent may etch the metal particles through the oxidation and reduction reactions, leaving merely silver salt on the substrate. X-ray diffraction measurements show AgCl crystals in the transparent areas after silver film treatment with either TBS containing NaCl and KCl or HCl 0.1-1 mM solution.[53] This redox process may affect the interface between the silver particles and the silicon dioxide, decreasing adhesion or even removing particles in solution. Deposition of the protein solution without buffer reveals no visible changes of the film surface in some cases, e.g. insulin, and might result in restructuring for other proteins, e.g. M2 monoclonal antibody. The specific dependence on protein properties is not established yet. Elemental analysis with X-ray photoelectron spectroscopy[52] show that the silver on the substrate is in the metal state (Ag 3d 5/2 peak at 368.5 eV) without oxidation during the first 2-3 weeks after fabrication while the metal is in an oxidized state about eight weeks after fabrication (the peak is shifted to 367.0 – 367.4 eV). Since many successful experiments were done with month-old ASFs, we conclude that the silver particles are covered with an

oxide layer initially and then deoxidize under deposition of protein molecules in buffer solution.

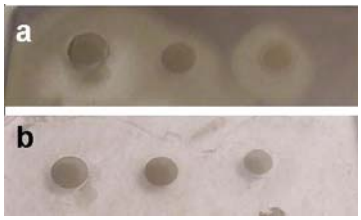

Figure 12-3. Photos of ASF substrate with insulin spots before (a) and after (b) washing with a Tris-buffered saline solution.

One more example of the restructuring mediated by M2 monoclonal antibody in TBS buffer solution is shown in Fig. 12-4b and by antigen in Fig. 12-4c. A lower concentration of protein results in lower metal coverage (the ratio of white area to total area in the FE SEM images). Fig. 12-4b and c show that a decrease of metal coverage correlates with the decreasing optical absorption (transmission T = 0.25 for 12-4b and T = 0.4 for 12-4c). Typically, protein solutions contain buffer. The effect of the protein concentration on silver film stabilization is illustrated in Fig. 12-5. A lower concentration of protein results in a lower metal particle surface density. The absorbance of the silver film is governed mostly by silver particles in the metal state. The absorbance increases with protein concentration and then saturates above a certain concentration which can be considered as optimal. The concentration dependence shows almost no change after 30 min of washing in TBS/Tween-20 solution (the circles in Fig. 12-5), which confirms the stabilization of the film by the proteins.

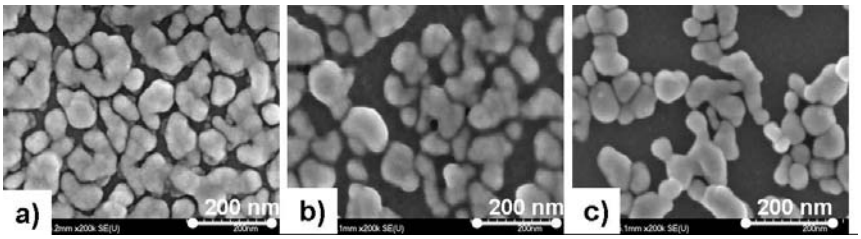

Figure 12-4. FE SEM images of two substrates from one batch: a) 12 nm silver film (transmission at 568 nm T= 0.27) ; b) 12 nm silver film inside Ab spot (T = 0.23-0.27); c) same substrate as b) but inside antigen (FLAG-BAP) spot (T = 0.4). Images were collected eight weeks after fabrication; proteins were deposited one week after fabrication.

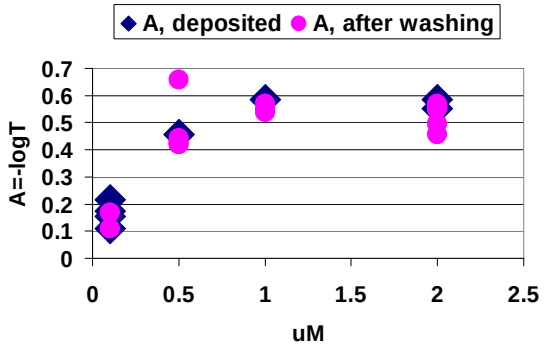

Figure 12-5. Absorbance at 568 nm inside protein spot (anti-interleukin 10) versus protein concentration.

SERS ENHANCEMENT

Depending on the mass thickness of the initial film, small or large fractal-like aggregates can be formed. The analyte SERS signal, normalized per metal mass coverage, is comparable for both the small (Fig. 12-3b) and large aggregates (Fig. 12-4b, c) that we examined. SERS enhancement is high enough to detect a monolayer of analyte.[49] Note that an aggregated structure provides conditions for both electromagnetic and chemical SERS enhancements. Even small aggregates provide strong electromagnetic enhancement in the visible and near infrared, as has been shown for polarization nonlinearities[58] and SERS.[31] Large aggregates typically have a fractal morphology, which is known to provide a particularly strong SERS signal.[22,39] In addition, the first molecular layer may also produce conditions to make an optical tunnel current possible, either through the molecule at the point of nearest approach between two particles,[59] or through a system operating as a molecular tunnel junction between particles across a vibrating molecular bridge.[60] Thus, adaptive feature of our films produces cavity sites enclosed by two or more particles, which are optimal for enhanced Raman. It is even more important that the cavity sites are naturally filled with proteins as a result of restructuring.

The measured macroscopic enhancement factor for insulin on our ASF substrate[49] relative to normal Raman of insulin on quartz is about 3×10^6. This is among the largest observed for random metal-dielectric films: 10^5 for nitrobenzonate[19] and 5.3×10^5 for *trans*-1,2-bis(4-pyridyl)-ethylene.[42]

A metal nanostructured film positioned near a mirror-like metal surface with a sandwiched dielectric layer has been employed to further increase SERS signal from ASF based biosensors.[52] Such a sandwich structure can show dramatic change in the film's optical properties.[61-63] The sandwich structure (Fig. 12-6b) contains a bulk silver layer (80 nm) deposited on glass, then a layer of SiO_2 (10 nm), and finally a 12 nm nano-structured silver film.

So, relative to the usual ASF (Fig. 12-6a) it has an additional sublayer of bulk metal. The bulk silver layer provides an additional enhancement of the local fields caused by interaction between particles and their images in the bulk layer and far-field interactions between particles. Test experiments with three analytes (human insulin, anti-human interleukin 10, and anti-human interleukin 10 incubated with 1 nM R6G) show that the multi-layer sandwich structure provides a signal increment of roughly 4-5 at least relative to the usual ASF.

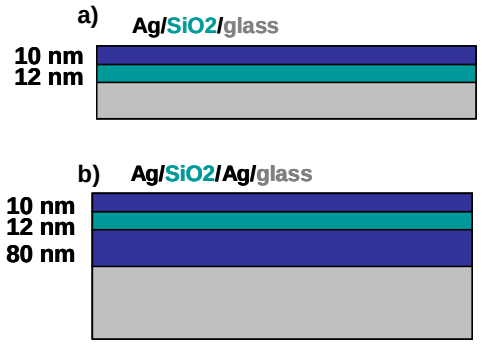

Figure 12-6. Vertical layer structure for ASF substrates: a) two-layer structure, b) multi-layer structure with an additional thick metal sublayer.

To summarize the above discussion, adaptive silver films allow protein-mediated restructuring of the metal nanoparticles, which makes it possible to address three issues. Specifically, proteins adsorb on the metal surface without significant structural changes (*soft*-adsorption), the silver film stabilizes which makes the analyte/metal combinations resistant to washing, and the SERS signal improves for given set of particles.

4. SERS OF INSULIN AND ANTIBODY-ANTIGEN BINDING DETECTION

We first discuss ASF experiments involving the detection of insulin analogs. Next we cover the detection of antibody-antigen binding events using ASF substrates.

In general, protein sensing using Raman spectroscopy provides important structural information on conformational changes. Changes between native and denatured insulin in the solid form as well as the spectral features of

proinsulin and insulin fibrils were studied previously.[64-66] Signatures of allosteric conformation changes in hexameric insulin have been assessed using Raman difference spectroscopy.[67]

Insulin is a protein consisting of 51 amino acids split into two chains (called A and B) and is a glucose regulation agent in the bloodstream. The experiments with adaptive substrates[49] examined the differences in Raman spectra of two insulin isomers, human insulin and its analog insulin lispro. These two insulins differ only in the interchange of two neighboring amino acids; specifically, the propyl-lysyl sequence at the C-terminus of the B-chain in insulin lispro is inverted as compared to human insulin. This propyl-lysyl switch leads to conformational changes at the C- and N-termini and has an important clinical effect for diabetes treatment. The difference in SERS spectra for the two insulins (see Fig. 12-7) was detected at a sub-monolayer density of 80 fmol/mm^2, with only 25 amol in the probed area.

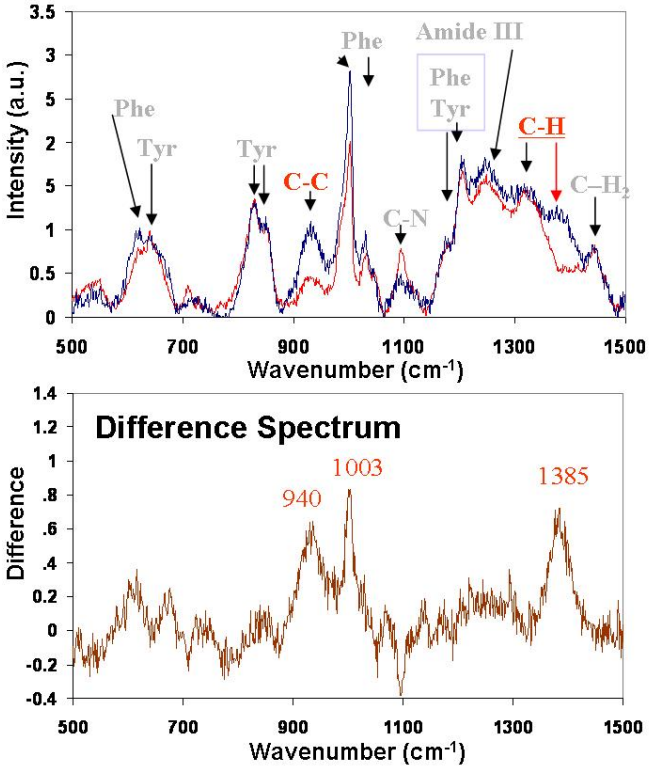

Figure 12-7. SERS spectra collected at 568 nm incident laser wavelength for human insulin (blue) and insulin lispro (red) on ASF substrates. The SERS difference spectrum (insulin – lispro) in the lower panel clearly shows the observed spectral differences between the two isomers.

A comparison of our SERS and normal Raman spectra for insulin on a quartz surface[50] and for Zn-insulin in solution[67] suggests that the SERS spectra reveal all known Raman fingerprint spectral peaks for insulin. The Raman peaks are assigned mainly to amide I and amide III bands of peptide backbone vibrations, to vibrational modes of Phe (located at the B1, B24, and B25 residues of the B-chain) and tyrosine (Tyr) (A14, A19, B16, and B26).[64]

The SERS difference between the two insulins can be attributed, in part, to i) Phe B1 displacement, and ii) the α-helical N-terminus of the B-chain in human insulin, which is a feature of the R-sate conformation. As mentioned, insulin is adsorbed on the surface primarily through the N-terminus. Because of the excess negative charge, metal particles attract the positively charged N-terminus of the B-chain and thus move Phe(B1) closer to the surface. Depending on the conformational state of the displaced Phe(B1), it can be at different distances and thus have different orientations with respect to the metal surface, enabling the observed increase in Phe peak intensities by a factor of 1.4 for human insulin as compared to insulin lispro. The CH deformation band at 1385 cm^{-1} and the C-C skeletal band at 940 cm^{-1} are stronger in human insulin than in insulin lispro. The 890-945 cm^{-1} band is a characteristic spectral line for an α-helix and is known to be sensitive to structural changes.[68-71] This spectral line is typically centered at 940 cm^{-1} and disappears or displays weak intensity upon conversion to β-sheet or random coil structures. It is also known that the C-H deformation band at 1371 cm^{-1} appears for the R_6 conformation of hexameric human insulin, which has the longest sequence (B1-B19) of α-helix.[67] We note that this band appears in R_6-T_6 Raman difference spectra and disappears in $T_3R^f_3$- T_6 spectra.[67] This points out the critical contribution of the α-helical residues Phe(B1), Val(2), and Ala(B3) at N-termini of R_6 hexamers in the C-H deformation band at 1370-1385 cm^{-1}. The observed differences in the SERS spectra suggest that human insulin and insulin lispro have different conformational states on the surface. Specific orientations of molecular bonds on the silver surface emphasize the SERS spectral difference between the two insulins, making the differences much stronger than for conventional Raman. The observed SERS spectral differences are in agreement with X-ray crystallographic studies of hexameric human insulin and insulin lispro.[72]

Since human insulin and its analog have the same set of side chains and differ only in conformational states, the observed difference reveals Raman features of the conformational state with the use of ASF substrates. In this study we used Raman difference spectroscopy, which is a general method of probing protein structure for comparison between closely related proteins,[73] which we extended to SERS in order to study the spectral features of insulin

conformation. In our experiments, all insulin vibration modes are enhanced by approximately the same factor. This makes the SERS spectra similar to the conventional Raman spectra in liquid and solid forms and simplifies the analysis.

We have also studied ASF substrates for use in antibody/antigen binding research. The detection of protein binding by optical means is of critical importance to current protein analysis, and promises to lead to a number of exciting future applications in biomedical diagnostics, research and discovery. The results show that SERS substrates based on ASFs allow direct, label-free SERS detection of antibody-antigen binding at a monolayer level. In experiments we used the following protocol. Antibodies (anti-FLAG M2 monoclonal antibody) were immobilized on ASF substrates to form a monolayer array, followed by incubation with an antigen solution at 1 nM concentration (C-terminal FLAG-BAP (bacterial alkaline phosphatase)). In each experiment, after the immobilization of antibodies and incubation with antigens the film was washed for about 20 min in a TBS/Tween-20 (as mentioned in Section 3) and then rinsed five times with deionized water. After washing, SERS spectra were collected to observe spectral changes following the incubation of antibodies with the antigen. Antigen-antibody binding events result in distinct SERS spectral changes as shown in Fig. 12-8 (blue – before incubation, red – after). In a control experiment incubation with BAP containing no FLAG reveals no spectral changes (Fig. 12-8, green spectra). It is important to note that ASF substrates allow independent *in situ* binding activity validation using traditional chemiluminescence and fluorescence methods. Such validation has been performed and confirms that antigens and antibodies retain their binding properties on our SERS-active substrate. As with insulin, we find that the deposited biomolecules (antibodies or antigens in this case) restructure and stabilize the ASFs so that the protein binding activities are preserved and, in parallel, SERS is improved.

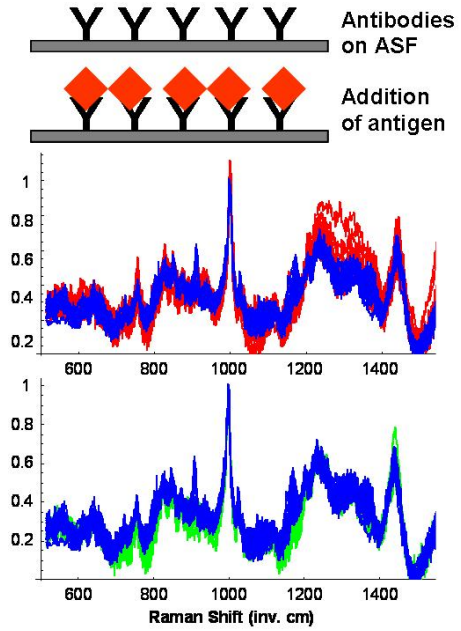

Figure 12-8. Antibody (anti-FLAG M2 monoclonal) and antigen (C-terminal FLAG-BAP) binding events. Spectra were taken before antigen incubation (blue) and after antigen incubation (red), nine spectra each. As a control experiment, non-binding BAP without FLAG was incubated on an antibody array, and the resulting SERS spectra (green) reveal no spectral changes.

Label-free detection using the ASF method produces unique advantages relative to prior optical binding detection methods (typically based on different types of labels) such as scintillation counting,[74] electrochemical,[75] enzymatic,[76] fluorescence,[76-78] and chemiluminescence methods.[79] An additional feature of ASFs is an ability to employ various detection methods on the same substrate, such as label-free SERS, chemiluminescence, and fluorescence.

ASF substrates used for protein microarrays reveal a promising opportunity to detect SERS spectra along with a fluorescence signal. Results from a microarray prepared using a quill-type spotter show that ASF substrates enable both fluorescence (with excitation at 633 nm) and SERS with no fluorescence (excitation at 568 nm) for the streptavidinCy5 fluorescence reporter.[52] SERS spectra of streptavidinCy5 can be used to distinguish between desirable and undesirable binding events. Since the interaction of biotin with streptavidin forms the basis of several widely used detection methods in bio-array technology, this application of SERS detection could be very important.

5. SUMMARY

Adaptive silver films allow protein sensing at monolayer surface density. The adaptive property of these substrates enables the adsorption of proteins without significant alteration in their conformational state. In an example using human insulin and insulin lispro, the results show that the SERS spectra reveal unique features attributable to distinct conformational states, which is in agreement with X-ray crystallographic studies. The experiments on protein array applications show evidence of distinct SERS spectral changes upon antigen-antibody binding using direct, label-free detection. Independent immunochemical assay validation confirms that the antibodies retain binding properties on ASFs. Experiments with a sandwich structure including a bulk metal layer below the ASF structure reveal a promising way to further improve the sensitivity of SERS-based biosensors.

ACKNOWLEDGEMENTS

We thank our colleagues E. N. Khaliullin, V. C. Nashine, D. Ben-Amotz, and V. J. Davisson for their contributions to the described work. This research was sponsored in a part by a grant from Inproteo.

REFERENCES

[1] M. Fleischmann, P.J. Hendra, and A.J. McQuillan, Raman spectra of pyridine adsorbed at a silver electrode, *Chem. Phys. Lett.* **26**, 163-166 (1974).

[2] D.J. Jeanmaire and R.P. Van Duyne, Surface Raman spectroelectrochemistry Part I. Heterocyclic, aromatic, and aliphatic amines adsorbed on the anodized silver electrode, *J. Electroanal. Chem.* **84**, 1-20 (1977).

[3] M.G. Albrecht and J.A. Creighton, Anomalously intense Raman spectra of pyridine at a silver electrode, *J. Am. Chem. Soc.* **99,** 5215-5217 (1977).

[4] T. Vo-Dinh, Surface-enhanced Raman spectroscopy using metallic nanostructures, *Trends Anal. Chem.* **17,** 557- 582 (1998)

[5] G. Bauer, N. Stich, and T.G.M. Schalkhammer, in: *Methods and Tools in Biosciences and Medicine: Analytical Biotechnology*, edited by T.G.M. Schalkhammer (Birkhauser Verlag Basel, Switzerland, 2002).

[6] M.S. Sibbald, G. Chumanov, and T.M. Cotton, Reductive properties of iodide-modified silver nanoparticles, *J. Electroanal. Chem.* **438,** 179-185 (1997).

[7] T. Vo-Dinh, D.L. Stokes, G.D. Griffin, M. Volkan, U.J. Kim, and M.I. Simon, Surface-enhanced Raman scattering (SERS) method and instrumentation for genomics and biomedical analysis, *J. Raman Spec.* **30,** 785-793 (1999).

[8] K.R. Brown, A.P. Fox, and M.J. Natan, Morphology-dependent electrochemistry of cytochrome c at Au colloid-modified SnO2 electrodes, *J. Am. Chem. Soc.* **118**, 1154-1157 (1996).

[9] K.E. Shafer-Peltier, C.L. Haynes, M.R. Glucksberg, and R.P. Van Duyne, Toward a glucose biosensor based on surface-enhanced Raman scattering, *J. Am. Chem. Soc.* **125,** 588-593 (2003).

[10] Y.W.C. Cao, R. Jin, and C.A. Mirkin, Nanoparticles with Raman spectroscopic fingerprints for DNA and RNA detection, *Science* **297,** 1536-1540 (2002).

[11] Y.C. Cao, R. Jin, J.M. Nam, C.S. Thaxton, and C.A. Mirkin, Raman dye-labeled nanoparticle probes for proteins, *J. Am. Chem. Soc.* **125,** 14676-14677 (2003).

[12] D.S. Grubisha, R.J. Lipert, H.Y. Park, J. Driskell, and M.D. Porter, Femtomolar detection of prostate-specific antigen: An immunoassay based on surface-enhanced Raman scattering and immunogold labels, *Anal. Chem.* **75,** 5936-5943 (2003).

[13] M. Moskovits, Surface-enhanced spectroscopy, *Rev. Mod. Phys.* **57**, 783- 826 (1985).

[14] M. Moskovits, Surface roughness and the enhanced intensity of Raman scattering by molecules adsorbed on metals, *J. Chem. Phys.* **69**, 4159-4161 (1978).

[15] C.Y. Chen, E. Burstein, and S. Lundquist, Giant Raman scattering by pyridine and Cn-adsorbed on silver, *Solid State Commun.* **32,** 63-66 (1979).

[16] S.L. McCall, P.M. Platzman, and P.A. Wolff, Surface enhanced Raman scattering, *Physics Lett.* **77A**, 381-383 (1980).

[17] C.Y. Chen and E. Burstein, Giant Raman scattering by molecules at metal island films, *Phys. Rev. Lett.* **45,** 1287-1291 (1980).

[18] J.G. Bergman, D.S. Chemla, P.F. Liao, A.M. Glass, A. Pinczuk, R.M. Hart, and D.H. Olson, Relationship between surface-enhanced Raman scattering and the dielectric properties of aggregated silver films, *Optics Lett.* **6**, 33-35 (1981).

[19] D.A. Weitz, S. Garoff, and T.J. Gramila, Excitation spectra of surface-enhanced Raman scattering on silver island films, *Optics Lett.* **7**, 168-170 (1982).

[20] G. Ritchie and C.Y. Chen, in: *Surface Enhanced Raman Scattering*, edited by P.K. Chang and T.E. Furtak (Plenum, New York, 1982), p. 361.

[21] G.C. Schatz, in: *Fundamentals and Applications of Surface Raman Spectroscopy,* edited by R.L. Garrell, J.E. Pemberton, and T.M. Cotton (VCH Publishers, Deerfield Beach, FL, 1993).

[22] M.I. Stockman, V.M. Shalaev, M. Moskovits, R. Botet, and T.F. George, Enahnced Raman scattering by fractal clusters – scale invariant theory, *Phys. Rev. B* **46,** 2821-2830 (1992).

[23] A. Otto, Raman-spectra of (CN)- adsorbed at a silver surface, *Surf. Science* **75**, L392-L396 (1978).

[24] I. Pockrand and A. Otto, Coverage dependence of Raman scattering from pyridine adsorbed to silver-vacuum interfaces, *Solid State Commun.* **35**, 861-865 (1980).

[25] B.N.J. Persson, On the theory of surface-enhanced Raman scattering, *Chem. Phys. Lett.* **82,** 561-565 (1981).

[26] F.J. Adrian, Charge transfer effects in surface-enhanced Raman scattering, *J. Chem. Phys.* **77,** 5302-5314 (1982).

[27] P.K.K. Pandey and G.C. Schatz, A detailed analysis of the Raman enhancement mechanisms associated with the interaction of a Raman scatterer with a resonant metal cluster: results for Li_n–H_2, *J. Chem. Phys.* **80,** 2959-2972 (1984).

[28] J.R. Lombardi, R.L. Birke, T. Lu, and J. Xu, Charge-transfer theory of surface enhanced Raman spectroscopy: Herzberg–Teller contributions, *J. Chem. Phys.* **84,** 4174-4180 (1986).

[29] A. Campion and P. Kambhampati, Surface-enhanced Raman scattering, *Chem. Soc. Rev.* **27**, 241-250 (1998).

[30] S. Nie and S.R. Emory, Probing single molecules and single nanoparticles by surface-enhanced Raman scattering, *Science* **275,** 1102-1106 (1997); Screening and enrichment of metal nanoparticles with novel optical properties, *J. Phys. Chem. B* **102,** 493-497 (1998).

[31] K. Kneipp, Y. Wang, H. Kneipp, L.T. Perelman, I. Itzkan, R.R. Dasari, and M. Feld, Single molecule detection using surface-enhanced Raman scattering (SERS), *Phys. Rev. Lett.* **78**, 1667-1670 (1997).

[32] G.C. Schatz and R.P. Van Duyne, in: *Handbook of Vibrational Spectroscopy*, edited by J.M. Chalmers and R.P. Griffiths (Wiley, New York, 2002), pp. 759-744.

[33] M.D. Musick, C.D. Keating, M.H. Keefe, and M.J. Natan, Stepwise construction of conductive Au colloid multilayers from solution, *Chem. Mater.* **9**, 1499-1501 (1997).

[34] A.M. Michaels, M. Nirmal, and L.E. Brus, Surface enhanced Raman spectroscopy of individual rhodamine 6G molecules on large Ag nanocrystals, *J. Am. Chem. Soc.* **121**, 9932-9939 (1999).

[35] C.L. Haynes and R.P. Van Duyne, Plasmon-sampled surface-enhanced Raman excitation spectroscopy, *J. Phys. Chem. B* **107,** 7426-7433 (2003).

[36] E. Prodan, C. Radloff, N.J. Halas, and P. Nordlander, A hybridization model for the plasmon response of complex nanostructures, *Science* **302,** 419-422 (2003).

[37] P. Gadenne, D. Gagnot, and M. Masson, Surface enhanced resonant Raman scattering induced by silver thin films close to the percolation threshold, *Physica A* **241,** 161-165 (1997).

[38] A.K. Sarychev and V.M. Shalaev, Electromagnetic field fluctuations and optical nonlinearities in metal-dielectric composites, *Phys. Reports* **335,** 275-371 (2000).

[39] V.M. Shalaev, in: *Nonlinear Optics of Random Media: Fractal Composites and Metal-Dielectric Films,* (STMP v.158, Springer, Heidelberg, 2000).

[40] J. P. Davies, S. J. Pachuta, R. G. Cooks, and M. Weaver, Surface-enhanced Raman-scattering from sputter-deposited silver surface, *J. Anal. Chem.* **58**, 1290 (1986).

[41] V.L. Schlegel and T.M. Cotton, Silver island films as substrates for enhanced Raman-scattering – effect of deposition rate on intensity, *Anal. Chem.* **63,** 241-247 (1991).

[42] R.P. Van Duyne, J.C. Hulteen, and D.A. Treichel, Atomic force microscopy and surface-enhanced Raman spectroscopy. I. Ag island films and Ag film over polymer nanosphere surfaces supported on glass, *J. Chem. Phys.* **99,** 2101-2115 (1993).

[43] E. Vogel, W. Kiefer, V. Deckert, and D. Zeisel, Laser-deposited silver island films: an investigation of their structure, optical properties and SERS activity, *J. Raman Spec.* **29,** 693-702 (1998).

[44] J.J. Mock, M. Barbic, D.R. Smith, D.A. Schultz, and S. Schultz, Shape effects in plasmon resonance of individual colloidal silver nanoparticles, *J. Chemical Physics* **116**, 6755-6759 (2002).

[45] M. Kerker, Electromagnetic model for surface-enhanced Raman scattering (SERS) on metal colloids. *Acc. Chem. Res.* **17**, 271-277 (1984).

[46] J.R. Krenn, A. Dereux, J.C. Weeber, E. Bourillot, Y lacroute, J.P. Goudonnet, G. Schider, W. Gotschy, A. Leitner, F.R. Aussenegg, and C. Girard, Squeezing the optical near-field zone by plasmon coupling of metallic nanoparticles, *Phys. Rev. Lett.* **82**, 2590-2593 (1999).

[47] E. Hao and G.C. Schatz, Electromagnetic fields around silver nanoparticles and dimmers, *J. Chemical Physics* **120**, 357-366 (2004).

[48] D.P. Fromm, A. Sundaramurthy, P.J. Schuck, G. Kino, and W.E. Moerner, Gap - dependent optical coupling of single "bowtie" nanoantennas resonant in the visible, *Nano Letters*, **4**, 957-961 (2004).

[49] V.P. Drachev, M.D. Thoreson, E.N. Khaliullin, V.J. Davisson, and V.M. Shalaev, Surface-enhanced Raman difference between human insulin and insulin lispro detected with adaptive nanostructures, *J. Physical Chemistry A*, **108**, 18046-18052 (2004).

[50] V.P. Drachev, M.D. Thoreson, E.N. Khaliullin, A.K. Sarychev, D. Zhang, D. Ben-Amotz, and V.M. Shalaev, Semicontinuous silver films for protein sensing with SERS, *SPIE Proceedings*, **5221**, 76-81 (2003).

[51] V.P. Drachev, V.C. Nashine, M.D. Thoreson, D. Ben-Amotz, V.J. Davisson, and V.M. Shalaev, Adaptive silver films for detection of antibody-antigen binding, *Langmuir*, submitted.

[52] V.P. Drachev, M.D. Thoreson, V.C. Nashine, E.N. Khaliullin, D. Ben-Amotz, V.J. Davisson, and V.M. Shalaev, Adaptive silver films for surface-enhanced Raman spectroscopy of biomolecules, *J. Raman Spec.*, to be published.

[53] V.P. Drachev, M.L. Narasimhan, H.-K. Yuan, M.D. Thoreson, Y. Xie, V.J. Davisson, and V.M. Shalaev, Adaptive silver films towards bio-array applications, *SPIE Proceedings,* **5703,** 13 (2005).

[54] P.B. Johnson and R.W. Christy, Optical constants of the noble metals, *Phys. Rev. B* **6**, 4370-4379 (1972).

[55] C. Kittel, *Introduction to Solid State Physics* (Wiley, New York, 1995).

[56] D.A. Genov, A.K. Sarychev and V.M. Shalaev, Surface plasmons excitation in semicontinuous metal films, in: *Progress in Condensed Matter Physics*, edited by F. Columbus (Nova Science Publishers, Hauppauge, NY, 2005).

[57] L. Eckertova, *Physics of Thin Films* (Plenum Press, New York and London, 1977).

[58] V.P. Drachev, S.V. Perminov, S.G. Rautian, and V.P. Safonov, in: *Optical Properties of Nanostructured Random Media*, edited by V.M. Shalaev (Topics in Applied Physics v. 82, Springer Verlag, Berlin, 2001), pp. 113-148.

[59] A.M. Michaels, J.J. Jiang, and L.E. Brus, Ag nanocrystal junctions as the site for surface-enhanced Raman scattering of single Rhodamine 6G molecules, *J. Phys. Chem. B* **104,** 11965-11971 (2000).

[60] S. Holzapfel, W. Akemann, D. Schummacher, and A. Otto, Variations of dc-resistance and SERS intensity during exposure of cold-deposited silver films, Surf Science, 1990, 227, p. 123-128.

[61] W.R. Holland and D.G. Hall, Frequency shifts of an electric dipole resonance near a conducting surface, *Phys. Rev. Lett.* **52,** 1041-1044 (1984).

[62] A. Leitner, Z. Zhao, H. Brunner, F.R. Aussenegg, and A. Wokaun, Optical properties of a metal island film close to a smooth metal suface, *Appl. Opt.* **32,** 102-110 (1993).

[63] H.R. Stuart and D.G. Hall, Enhanced dipole-dipole interaction between elementary radiators near a surface, *Phys. Rev. Lett.* **80,** 5663-5666 (1998).

[64] N.-T. Yu and C.S. Liu, Laser Raman spectra of native and denatured insulin in the solid state, *J. Am. Chem. Soc*. **94**, 3250-3251 (1972.).

[65] N.-T. Yu, C.S. Liu, and D.C O'Shea, Laser Raman spectroscopy and the conformation of insulin and proinsulin, *J. Mol. Biol.* **70,** 117-132 (1972).

[66] N.-T. Yu, B.H. Jo, R.C.C. Chang, and J.D. Huber, Single-crystal Raman spectra of native insulin: structures of insulin fibrils, glucagon fibrils, and intact calf lens, *Arch. Biochem. Biophys.* **160,** 614-622 (1974).

[67] D. Ferrari, J.R. Diers, D.F. Bocian, N.C. Kaarsholm, and M.F. Dunn, Raman signature of ligand binding and allosteric conformation change in hexameric insulin, *Biopolymers (Biospectroscopy)*, **62**, 249-260 (2001).

[68] T.-J. Yu, J.L. Lippert, and W.L. Peticolas, Laser Raman studies of conformational variations of poly-l-lysine, *Biopolymers* **12**, 2161-2176 (1973).

[69] M.C. Chen, R.C. Lord, and R. Mendelson, Laser-excited Raman spectroscopy of biomolecules 4: thermal denaturation of aqueous lysozyme, *Biochem. Biophys. Acta* **328**, 252-260 (1973).

[70] B.G. Frushour and J.L. Koenig, Raman spectroscopy study of tropomyosin denaturation, *Biopolymers* **13**, 1809-1819 (1974).

[71] M.C. Chen, R.C. Lord, and R. Mendelson, Laser-excited Raman spectroscopy of biomolecules 5: conformational changes associated with chemical denaturation of lysozyme, *J. Am. Chem. Soc*. **96**, 3038-3042 (1976).

[72] E. Ciszak, J.M. Beals, B.H. Frank, J.C. Baker, N.D. Carter, and G.D. Smith, Role of C-terminal B-chain residues in insulin assembly: the structure of hexameric $Lys^{B28}Pro^{B29}$-human insulin, *Structure* **3**, 615-622 (1995).

[73] R. Callender, H. Deng, and R. Gilmanshin, Raman difference studies of protein structure and folding, enzymatic catalysis and ligand binding, *J. Raman Spec.* **29,** 15-21 (1998).

[74] S. Gutcho, and L. Mansbach, Simultaneous radioassay of serum vitamin-B12 and folic acid, *Clin. Chem.* **23,** 1609-1614 (1977).

[75] F.J. Hayes, H.B. Halsall, and W.R. Heineman, Simultaneous immunoassay using electrochemical detection of metal-ion labels, *Anal. Chem.* **66,** 1860-1865 (1994).

[76] J.E. Butler, Enzyme-linked immunosorbent assay, *J. Immunoassay* **21,** 165-209 (2000).

[77] J. Vuori, S. Rasi, T. Takala, and K. Vaananen, Dual-label time-resolved fluoroimmunoassay for simultaneous detection of myoglobin and carbonic acnhydrase-III in serum, *Clin. Chem.* **37,** 2087-2092 (1991).

[78] Y.Y. Xu, K. Pettersson, K. Blomberg, I. Hemmila, H. Mikola, and T. Lovgren, Simultaneous quadruple-label fluorometric immunoassay of thyroid-stimulating hormone, 17-alpha-hydroxyprogresterone, immunoreactive trypsin, and creatine-kinase MM isoenzyme in dried blood spots, *Clin. Chem.* **38,** 2038-2043 (1992).

[79] C.R. Brown, K.W. Higgins, K. Frazer, L.K. Schoelz, J.W. Dyminski, V.A. Marinkovich, S.P. Miller, and J.F. Burd, Simultaneous determination of total IgE and allergen-specific IgE in serum by the MAST chemi-luminescent assay system, *Clin. Chem.* **31,** 1500-1505 (1985).

[80] D. A. Genov, A.K. Sarychev, V.M. Shalaev, and A. Wei, Resonant Field Enhancement from Metal Nanoparticle Arrays, Nano Letters, **4**, NL-0343710 (2004).